NIPES

Journal of Science and Technology Research

Journal homepage: www.nipesjournals.org.ng

Performance Analysis of Induction Motor with Variable Air-Gaps using Finite Element Method

Onwuka, I. K[a], Obi, P.I[*a], Oputa, O[a] and Ezeonye, C.S[b]

[a]*Department of Electrical/Electronic Engineering, Michael Okpara University of Agriculture, Umudike, Abia State, Nigeria*
[b]*Department of Electrical/Electronic Engineering, University of Agriculture and Environmental Sciences, Umuagwo, Imo State, Nigeria*
[a]*onwuka.ifeanyichukwu@mouau.edu.ng* [*a]*patndyobi@gmail.com* [a]*connectositao@gmail.com*
[b]*ezeonyechinonso@yahoo.com*

Article Info

***Keywords*:**
Air-Gap, Efficiency, Induction Motor, Magnetizing current, Torque

Received 16 December 2022
Revised 05 January 2023
Accepted 06 January 2023
Available online 13 March 2023

https://doi.org/10.5281/zenodo.7729203

Abstract

In this study, three models of induction motor (IM) were used to examine the effect of different air-gaps (0.3 mm, 0.5 mm, and 1.0 mm) which have the same electrical features. One of these is the standard 3-phase, 1.5 kW, wye connected motor and the others are modified motors which have different diameters. The torque, efficiency and ripple values of each model were calculated using Finite Element. It was observed that the model with 1.0 mm has lower efficiency of 88.4% compared with the other efficiencies of 94% and 92%. Also, lower power factor values of 0.92 and 0.95 were obtained at 0.7 mm and 1.0 mm gaps respectively while highest power factor of 0.97 were obtained at 0.3 mm gap at the same speed of 1360 rpm. Furthermore, it was observed that increase in the gap increases the magnetizing current produced in the gap from 3 A to 4.36 A at rated conditions. Besides, losses were increased from 73.7 W to 91.4 W while the torque ripples increased from 4.15% to 4.74%. Considering the reliability and efficiency of the motor, the prime value of the air-gap thickness should be between 0.3 – 0.5 mm for the studied motor. Hence, there is need for the designer of induction motor to maintain the minimum air-gap length in order to improve the power factor and to reduce the no-load losses in the motor.

1. Introduction

Induction motor is the type of alternating current (AC) motor that is mostly used for appliances, automation and industrial applications due to its reliability, durability, robustness and high efficiency [1, 2]. It operates on the concept of interaction of the stator magnetic rotating field on currents induced in the rotor winding. It has some features as high efficiency, high rated power, minimum starting torque, low copper loss, reduced noise and vibration [3 – 5]. This type of AC motor comprises of two different types of rotor which can be placed inside the stator that is, cage rotor winding and wound rotor winding with slip rings as can be seen in Figure 1 [6, 7].

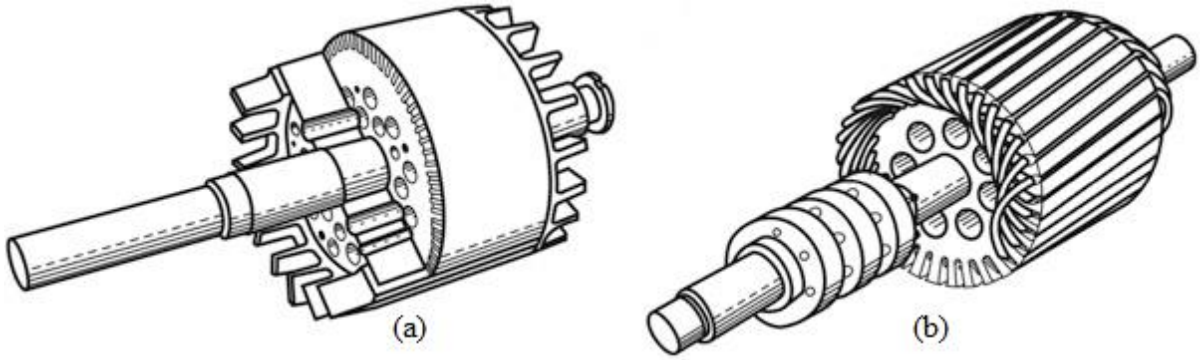

Figure 1: (a) Cage rotor and (b) Wound rotor induction motor rotor types [8]

The stator is made of a laminated silicon steel sheets with evenly stamped in slots to accommodate three-phase winding suitably connected to form a balanced three-phase star or delta connected circuit [9]. The stator contains six slots per pole pair, in each case one for the forward and one for the backward conductor for each phase winding. Generally, the winding is carried out with many pole pairs and distributed in different slots [10]. The cage rotor type of IM is made of laminated cylindrical core with parallel slots on its outer periphery with one copper bar or aluminum placed on each slot and close to the rotor surface. It comes with no brush or slip rings so it needs lower maintenance [11, 12]. The wound rotor is also made of a laminated cylindrical core and bears a three-phase winding similar to that of stator except the number of slots is smaller with fewer turns per phase. The wound rotor winding is mostly star connected and is distributed uniformly in the slots. The winding open end is brought out and fixed to three insulated slip rings set up on the rotor shaft with one brush resting on each of the slip ring. These slip rings are insulated from one another and from the motor shaft. A variable amount of external resistance can be connected to the rotor windings through the slip rings in order to have higher amount of starting torque [13]. The rotor and stator are separated by a small air-gap ranging from 0.4 mm to 4 mm, depending on the motor power [14].

The operation of three-phase IM is established on the application of Faraday's law and Lorentz force on a conductor. This depends on the rotating magnetic field set up by the stator current in the motor air-gap when energized with a three-phase supply. When the three-phase stator winding of an induction motor is connected to a three-phase supply, current will flow in each phase. These currents are time displaced from each other by 120 electrical degrees in a space around the inner circumference of the stator in a two-pole machine [15]. Due to the phase difference of the winding currents and the winding spacing, the pulsating or sinusoidally distributed magnetomotive force (MMF) produced by each phase combines to form a resulting MMF, which circulates around the air-gap at a synchronous speed. The rotating magnetic field sweeps through the air-gap and cuts the rotor windings. The relative speed between the resulting flux and the rotor causes emfs to be induced in the rotor windings thereby, current flows through the rotor conductors since the rotor circuit is short-circuited. The sum of MMF on the rotor conductors generates a torque which tends to move the rotor in the direction of flux [16, 17].

Several recent studies were carried out on the analysis of induction motor. Performance investigation of three phase induction machine resulting from axial non-uniform air-gap known as static eccentricity was carried out by [18] with the aid of modified winding function approach. Similarly, [19] performed modelling of eccentricity in three-phase induction motor, where they utilized its geometries to evaluate the inductances and electromagnetic torque for performance improvement of the motor. [20] used a 2D electromagnetic model to evaluate the operating

performance of a 1.5 kW induction motor through magnetic properties of core. Performance analysis of 3-phase, 5-phase, 7-phase and 9-phase squirrel cage induction motors were carried out by [21] on the basis of variation of the magnetic field along the middle circle of the air-gap and the time harmonics of the motor's torque and stator currents. Comparative analysis between three-phase and six-phase induction motor with the aid of direct torque control (DTC) based algorithm was carried out by [22]. They based the analysis on torque response under variable and fixed load condition. Analysis and modelling of thermal and electromagnetic behaviour of an IM using finite element analysis (FEA) was presented by [23]. This is done for design and accurate prediction and approximation of electromagnetic torque, magnetic flux, stator and rotor losses of induction motor for application in various industries. [24] used voltage source finite element method to determine the equivalent circuit variables by performing simulation on the no-load and locked-rotor test of a single-phase induction motor.

A lot of researchers have executed work on analysis of an IM in different perspectives as has been depicted including effect of air-gap on the behaviour of the motor but none has done holistic approach which involves different variabilities to the best of the authors' knowledge. This work therefore involves detailed performance analysis of IM including thermal index, torque ripple effect, and current harmonics of the phase current, etc, by the use of numerical technique.

2. Methodology

The IM has a stator and the rotor as its major parts as presented in Figure 2. The stator is a stationary part and the rotor is a rotating part. Figure 2(a) shows image of 1.5 kW IM in the machine laboratory of Department of Electrical/Electronic Engineering, Michael Okpara University of Agriculture Umudike.

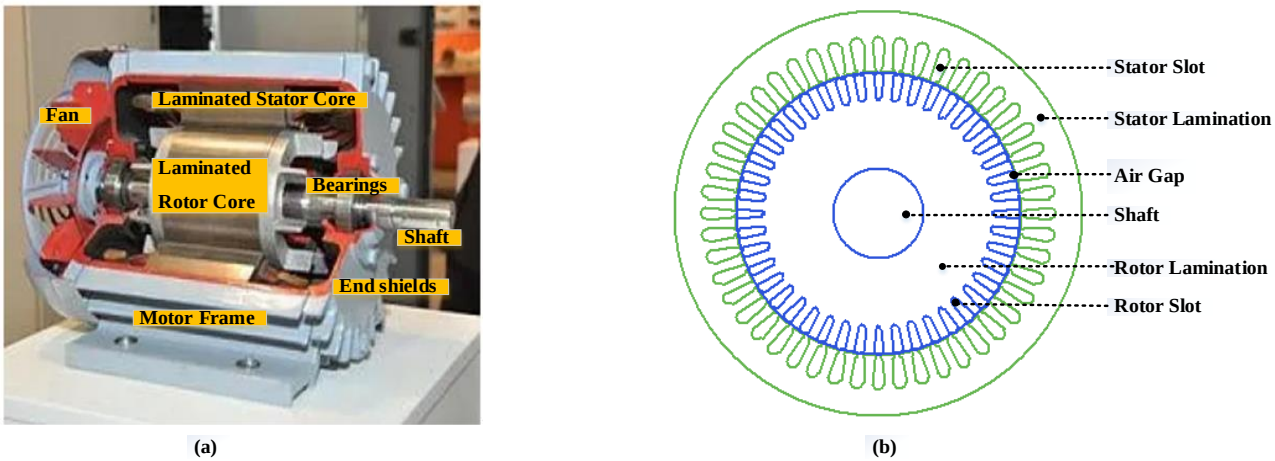

Figure 2: Diagram of the motor (a) Image of 1.5 kW Induction Motor (b) Typical parts of Induction Motor

The stator of the motor has overlapping coils that are physically placed 120-degree electrical apart. When the stator is connected to the three-phase power supply, a rotating magnetic field of constant magnitude and a varying direction is set up. The flux set up in the stator moves through the air-gap and gets linked to the rotor conductors. Figure 2(b) shows the other parts of the 2D model of the motor in RmxPrt. The geometric parameters of the motor are presented in Table 1. M-I, M-II, and M-III represent the motor with air-gaps of 0.3 mm, 0.5 mm, and 0.7 mm, respectively.

Table 1: Geometric parameters of the motor

GEOMETRIC COMPONENTS	VALUES		
	M-I	**M-II**	**M-III**
Stator external diameter	210 mm	210 mm	210 mm
Stator internal diameter	147.8 mm	148 mm	148 mm
Rotor external diameter	147.5 mm	147.5 mm	147.3 mm
Rotor internal diameter	48 mm	48 mm	48 mm
Axial length	250 mm	250 mm	250 mm
Stator conductors per slot	15	15	15
Number of stator slot	48 slots	48 slots	48 slots
Number rotor slot	44 slots	44 slots	44 slots
Stacking factor	0.92	0.92	0.92
Steel Type	M19-24G	M19-24G	M19-24G
Slot type	2	2	2

2.1 Establishment of Finite Element Models of the Motor

The numerical method adopted in this paper is the finite element (FE) technique. It is well suited for the analysis involved with nonlinearities and can be used for solving both linear and non-linear field problems including simple and complex geometries [25 – 27]. Field solution of the motor can be represented by solving these Maxwell's equations subjected to certain boundary conditions:

$$\nabla \times \mathrm{H} = \mathrm{J} + \frac{\delta \mathrm{D}}{\delta \mathrm{t}} \quad (1)$$

$$\nabla \times \mathrm{E} = -\frac{\delta \mathrm{B}}{\delta \mathrm{t}} + \nabla \times (\mathrm{v} \times \mathrm{B}) \quad (2)$$

$$\nabla . D = \rho \quad (3)$$

$$\nabla . \mathrm{B} = 0 \quad (4)$$

Where E, D, H, B, J,*v*, ρ, – represent the electric field intensity and electric flux density respectively, magnetic field intensity and magnetic flux density, current density, velocity of the conductor, and electric charge density, respectively.

In the analysis of electrical machines, the displacement current, $\frac{\delta \mathrm{D}}{\delta \mathrm{t}}$, in Equation (1), is disregarded since the frequencies of interest are usually low enough that the displacement current is negligible. In addition to the Maxwell's equations, there are constitutive relations, which describe the properties of the material over which the electromagnetic field is to be solved. These relations are,

$$\mathrm{D} = \mathcal{E}\mathrm{E} \quad (5)$$

$$\mathrm{B} = \mu\mathrm{H} \quad (6)$$

$$\mathrm{J} = \sigma\mathrm{E} \quad (7)$$

where $\mathcal{E}$, μ, and σ denote the permittivity, magnetic permeability, and the conductivity of the material respectively.

The transient solver and the static magnetic field solver are used in Ansoft Maxwell software, and the 3-phase motor will be simulated and analysed in this paper. The number of poles is four, the rated power, and voltage are respectively 1.5 kW and 380 V. The stator windings and the rotor cage (bars-end rings) are made respectively with copper and aluminium materials. The finite element model of the motor will be established before the analysis, and it is shown in Figure 3.

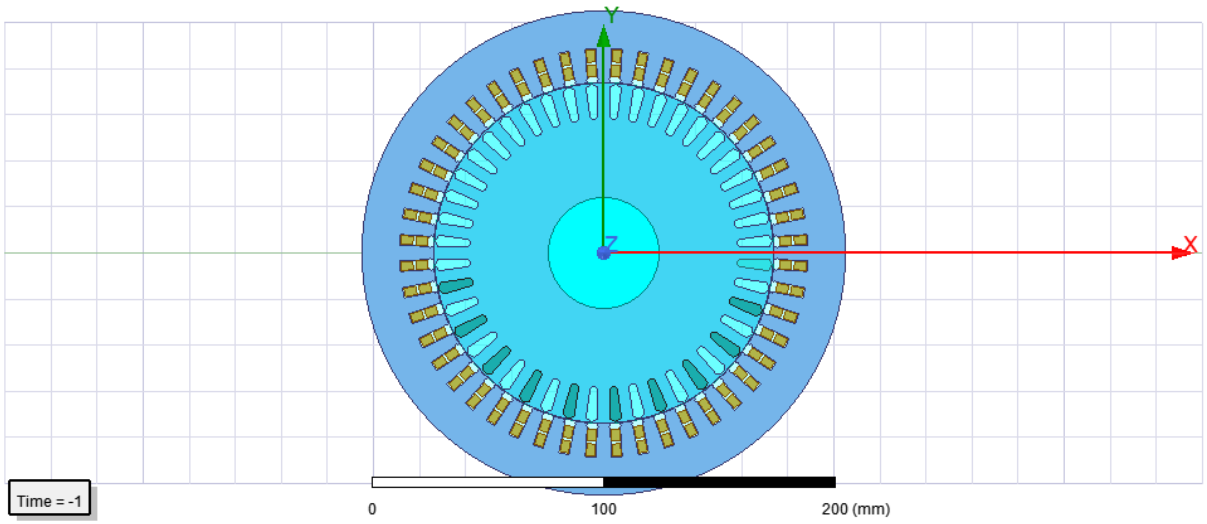

Figure 3: Finite element model of the studied motor

Stator slot the motor is shown in Figure 4 with its parameters shown in Table 2.

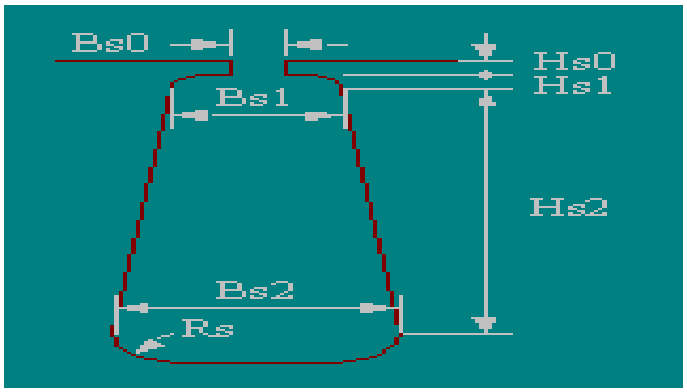

Figure 4: Stator slot of the motor

Table 2: Slot Dimensions

Slot Dimension	Values (mm)
Hs0	0.8
Hs1	1.05
Hs2	12.9
Bs0	2.8
Bs1	4.9
Bs2	6.7

2.2 Discretization of the FE Meshes

The discretization of the studied motor model is made through mesh division, and its quantity directly influences the arithmetical result of the FE approach. The largest change in magnetic field rate is air-gap; thus, the mesh in this area should be divided with higher density. The mesh division on the poles of the motor should also be given great concern as shown in Figure 5.

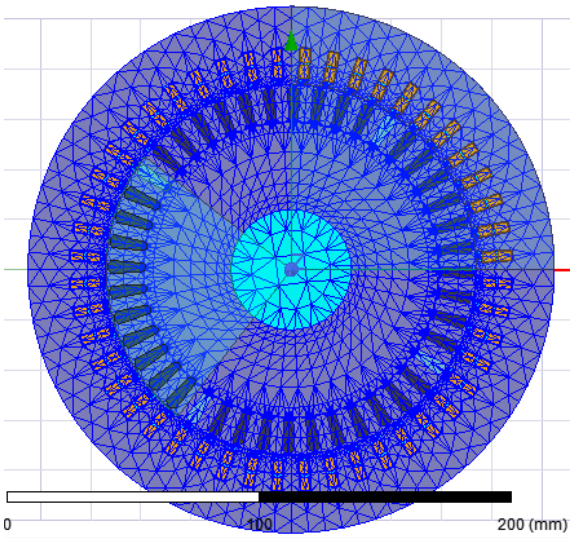

Figure 5: Meshed model of the motor

Figure 5 shows that there are 93, 716 mesh divisions. The pre-established motor will be simulated after setting up all the data.

3. Results and Discussion

In this section, three models (M-I, M-II, and M-III) of the induction motor were obtained and implemented in the Ansys Maxwell environment.
Two-dimensional (2D) FEA was performed using the ANSYS 2020 electromagnetic package. The full-pitched three-phase main windings were excited by three-phase sinusoidal voltage. Skin effect and core loss were considered in the FEA. Due to the symmetry of the motor, only pole pitch was considered in the FEA. Figures 6 – 8 show the flux density distribution in the core of the motor with air-gap lengths of 0.3 mm, 0.5 mm, and 0.7 mm for M-I, M-II, and M-III, respectively. The vector boundary condition with zero vector potential was set to the outer region of the machine's model. The edges of the 2D Cartesian coordinate area were modelled with a master boundary condition on the x-axis and a slave boundary condition on the y-axis. The field values of the three models are shown in Table 3.

Table 3: Field values of the three models

Properties	**M-I**	**M-II**	**M-III**
Flux lines (x 10^5 A/m)	5.1411	4.3744	4.0269
RMS magnetizing current (A)	3	3.64	4.36
Total loss (kW)	0.0737	0.0811	0.0914
RMS current density (A/mm^2)	3.13	3.48	3.88

The flux density distributions of three models at stop time of 140 ms are presented in Figures 6 – 8.

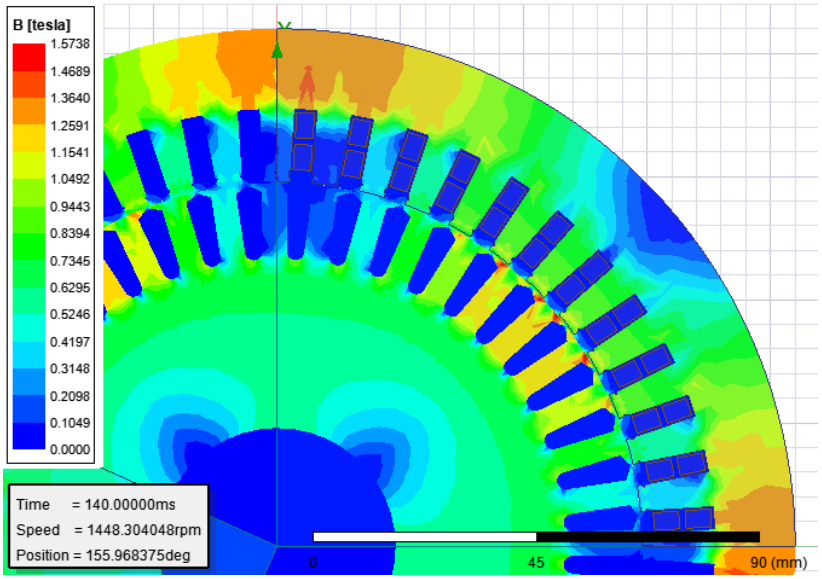

Figure 6: Distribution of flux density of M-I

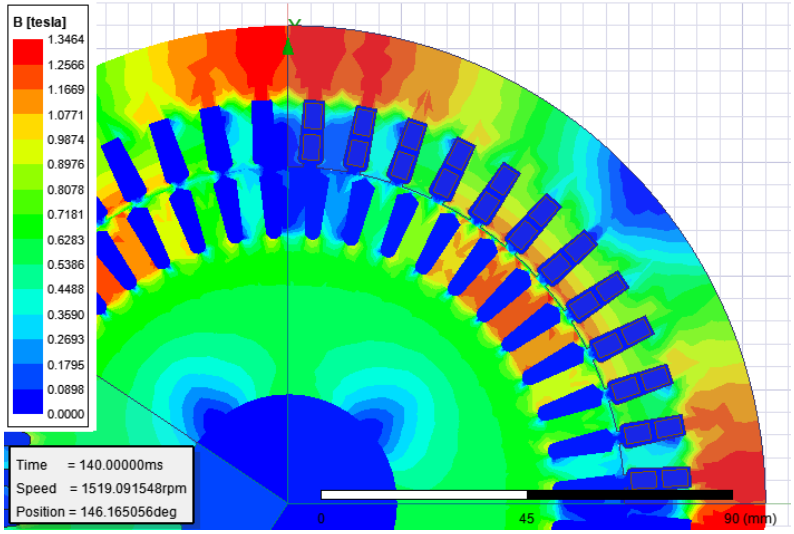

Figure 7: Distribution of flux density of M-II

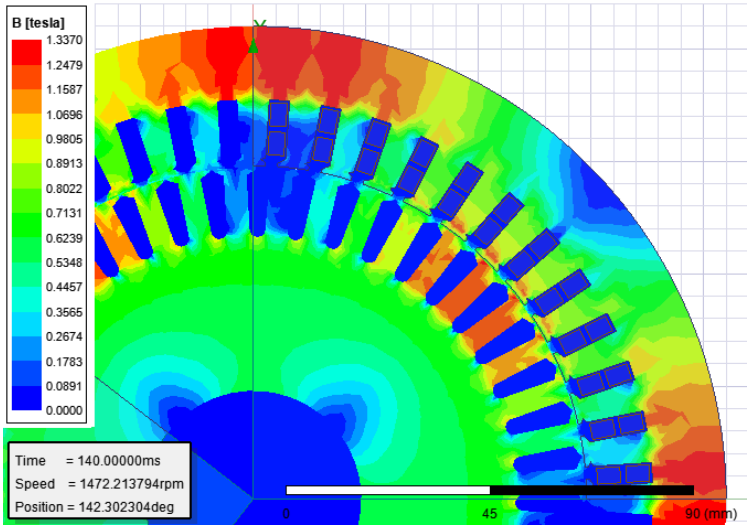

Figure 8: Distribution of flux density of M-III

At stop time of 140 ms, the whole magnetic field is uniformly distributed, the outer rotor moves and the magnetic flux density shows a periodic change. The motor in loading state influences the change in magnetic flux density. Since air-gaps are integral part of gapped inductors, the gap decreases effective magnetic circuit permeability and allows storing much greater energy before reaching saturation. It can be observed that M-I recorded the highest flux density of 1.5738 T, followed by M-II with 1.3454 T and M-III with 1.3370 T. Increased air-gap length in M-III reduces the inductance which means reduced flux density, so the winding needs more turns to compensate accordingly.

The basic comparative properties of the three models are shown in Figure 9.

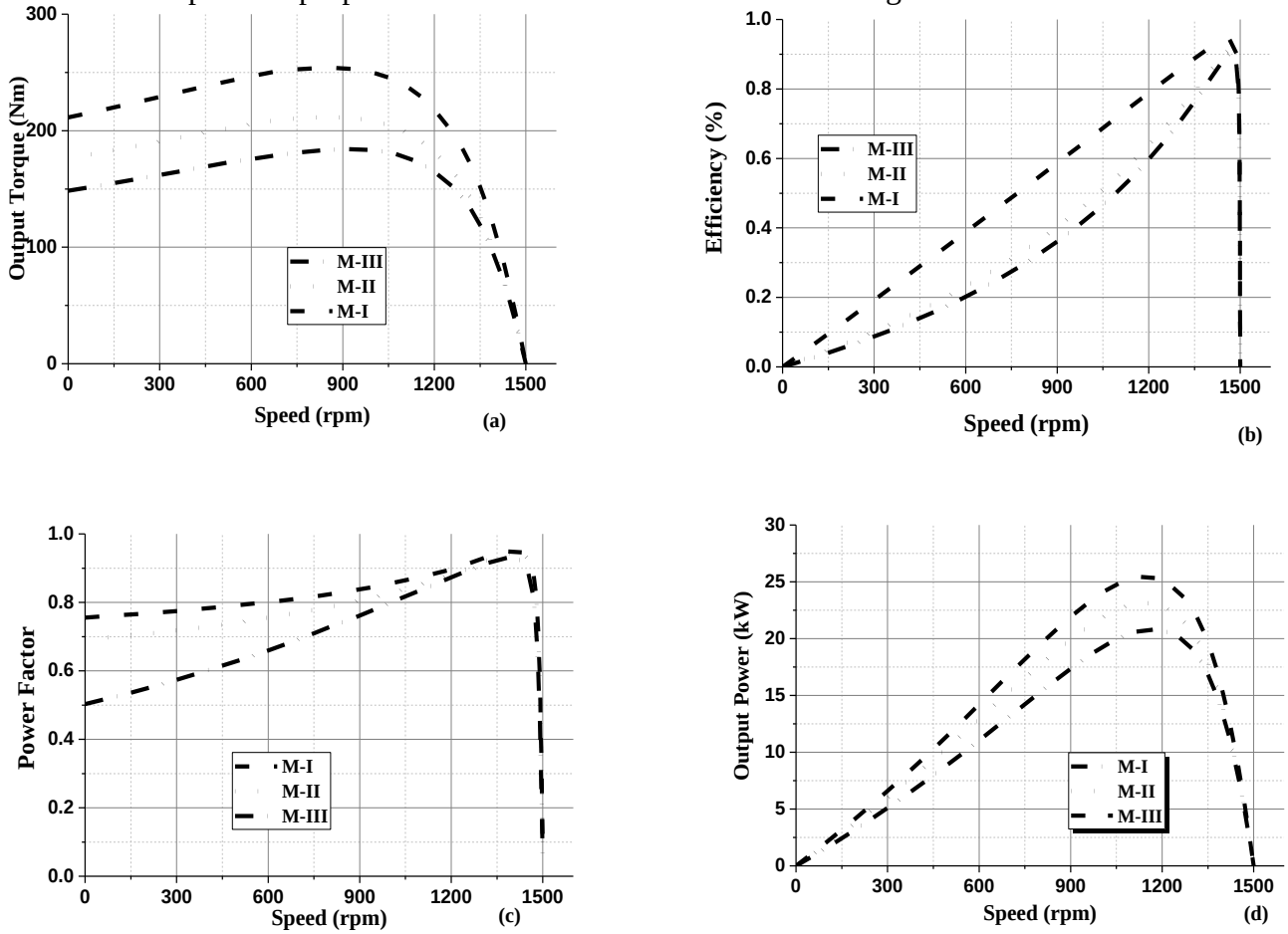

Figure 9: Basic comparative characteristics of the three models

M-III has the lowest output torque of 182Nm at 900 rpm when compared with M-II and M-I with 210.3Nm and 251Nm respectively as plotted in Figure 9a. This is because as the air-gap of M-III is increased to 1mm, the flux linkage will decrease, so, less emf will be generated. As per Lenz Law, the torque which will be produced by the emf so as oppose the flux, will be reduced. M-III has lower efficiency of 88.4% compared with M-II and M-I with efficiencies of 92% and 94% respectively as shown in Figure 9b. This is because M-III has the widest air-gap of 1 mm which led to a weaker magnetic circuit (as observed in magnetic flux density plot of Figure 8) and reduced efficiency of the motor. M-III and M-II have lower power factor values of 0.92 and 0.95 respectively while M-I recorded highest power factor of 0.97 at the same speed of 1360 rpm as shown in Figure 9c. This is because as the induction motor air-gap increases, the magnetizing current increases which leads to increase in the magnetic circuit reluctance. This reluctance increase will request more magneto-motive force (MMF) to produce the flux required in the motor. In order meet the additional requirement of MMF, the magnetizing current of the stator increases which led to the decreased in

power factor of the M-III. Figure 9d shows that the lesser the air-gap, the more power will be transferred. From Figure 9d, the output power of M-I, M-II, and M-III at 1080 rpm are 25.6 kW, 22.8 kW, and 20.8 kW, respectively. With an increase in air-gap length in M-III, the more magnetizing current is required to produce the rated flux in its magnetic core, and the phase angle between the applied voltage and the magnetizing current increases. As a result, the output power becomes low.

The thermal lumped parameters of the models are presented in Table 4 while the percentage total loss exhibited by the individual model is shown in Figure 10.

Table 4: Thermal lumped parameters of the models

Thermal Properties	**M-I**	**M-II**	**M-III**
Thermal resistance (^{0}C/W)	0.613	0.606	0.596
Average heat capacity (J/^{0}C)	10984	10964	10944
Average steady-state temp. (^{0}C)	32.1	34.2	36.5

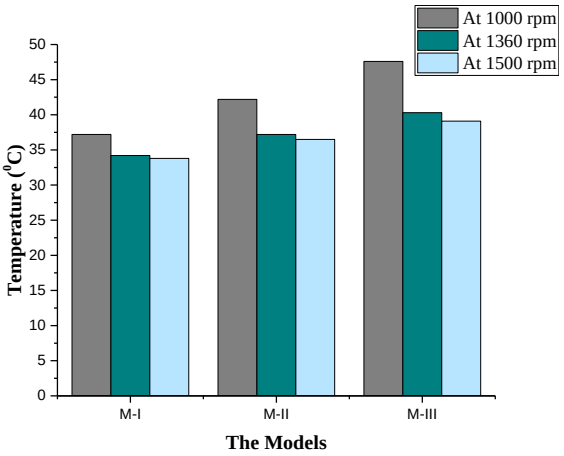

Figure 10: Temperature chart of the models at different speeds

It can be found that when the air-gap thickness is 1 mm (M-III) as seen in Figure 10, the maximum temperature inside the stator reaches 47.6^0 at 1000 rpm, which seriously affects the reliability and life span of the motor in a continuous low speed region. Therefore, in considering the motor reliability and efficiency, the maximum value of the air-gap thickness should be between 0.3 – 0.5 mm.

The dynamic speed results of the models are presented in Figure 11.

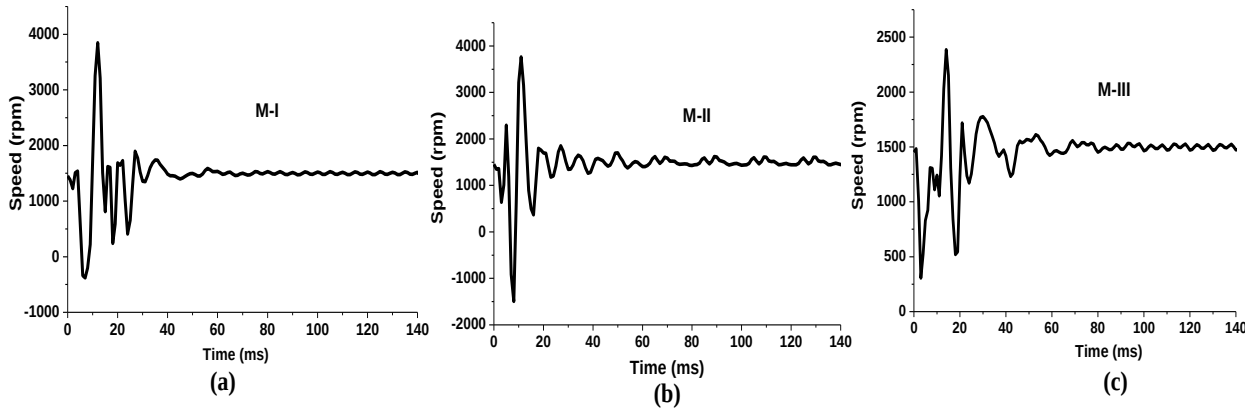

Figure 11: Dynamic speed results of the models

From Figure 11, it can be observed that the speed was oscillating around 1500 rpm but with different settling times of 60 ms, 62 ms, and 80 ms, in Figure 11a, 11b, and 11c, respectively. The inrush speed of M-III was observed to be 2390 rpm which is lower than 3770 rpm and 3700 rpm of M-I and M-II respectively. This is because increase in the air-gap of M-III led to decrease in the flux linkage which resulted to less generated emf. This will result in decrease in its speed.

The 3-phase currents of the models are presented in Figures 12.

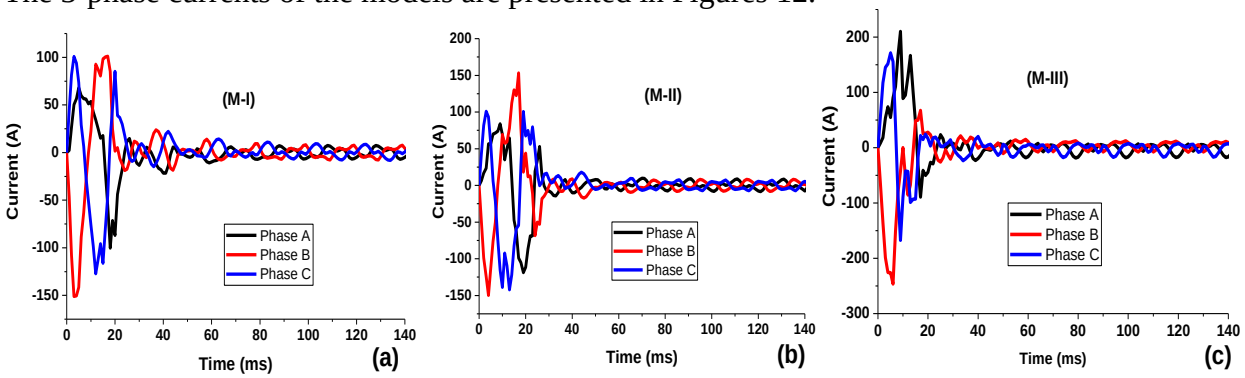

Figure 12: Dynamic phase current results of the models

In Figure 12, the inrush currents and steady state current values at 50 ms of M-I, M-II, and M-III were observed to be 100A/11A, 150A/13A, and 200A/18A, respectively. It can be seen that M-III has the highest steady state current of 18 A at 50 ms because motor phase currents depend on the air-gap length of the machine and the specific electric loading. A large air-gap length leads to higher phase current.

The torque characteristics of the models at rated condition are shown in Figures 13.

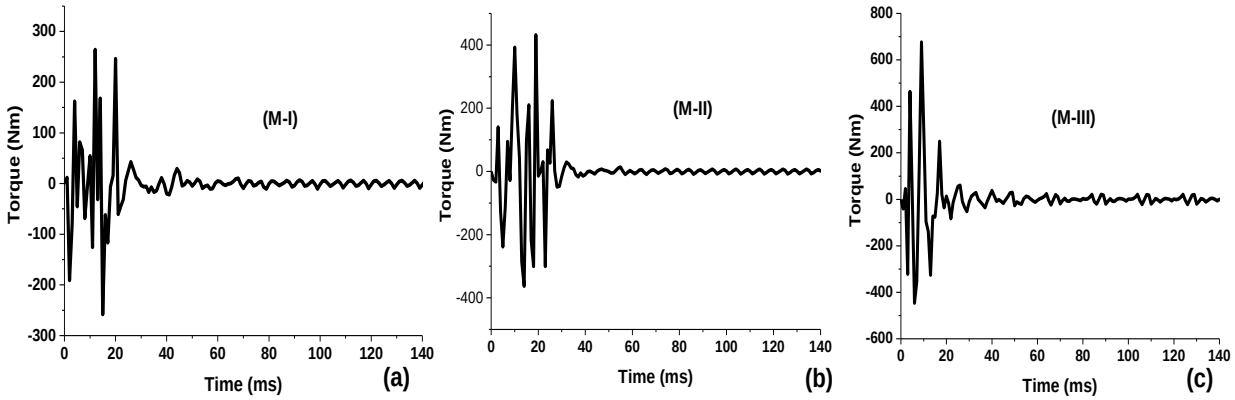

Figure 13: Dynamic torque results of the models

The starting torque of M-I, M-II, and M-III were obtained as 251 Nm, 400 Nm, 680 Nm, respectively. M-III has the highest starting torque because it has the largest air-gap of 1mm which led to increased reluctance of magnetic circuit, and the magnetic current consumption would be increased with more leakage flux.

The current harmonics and torque ripple of the models at different operating speed are shown in Figures 14 and 15 respectively.

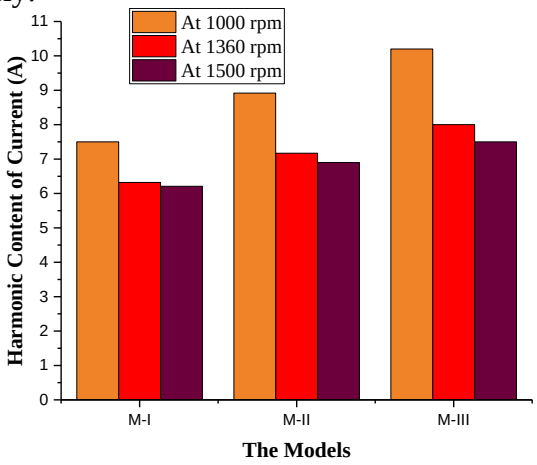

Figure 14: Harmonic content of current of the models at different speeds

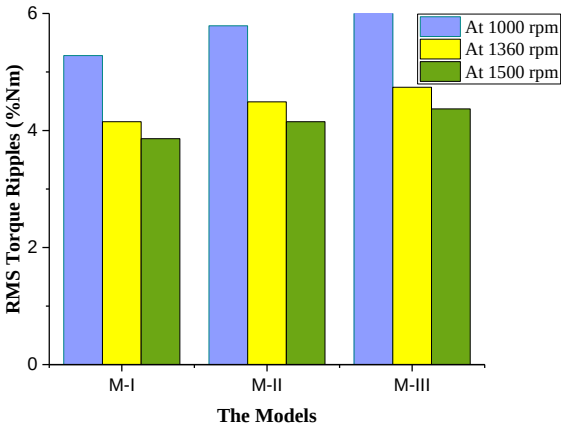

Figure 15: RMS torque ripple of the models at different speeds

From Figure 14, It can be observed that the current harmonics were increased by increasing the air-gap length. Accordingly, the harmonic effects such as torque ripple were increased as seen in Figure

15. Therefore, in considering the motor reliability and efficiency, the optimum value of the air-gap thickness should be between 0.3 – 0.5 mm.

4. Conclusion

The impact of thickness of the air-gap on the motor performance was analysed and studied, which is of great importance for the further and future advancement of the motor performance and the improvement of the material. During the study, the thickness of the air-gap was varied from 0.3 mm to 1.0 mm. It was observed that the model with 0.3 mm gap length obtained the highest flux density of 1.5738 T, while model of 1 mm gap length recorded 1.3370 T. Increased air-gap length in the latter reduces the inductance which means reduced flux density, so the winding needs more turns to recompense accordingly. Furthermore, it was observed that increase in the air-gap increase the magnetizing current produced in the air-gap from 3 A to 4.36 A at rated conditions. Besides, losses were increased from 73.7 W to 91.4 W while the torque ripples increased from 4.15% to 4.74%. Considering the motor reliability and efficiency, the optimum value of the thickness of air-gap should be between 0.3 – 0.5 mm. Hence, there is need for the designer of induction motor to maintain the minimum air-gap length in order to improve the power factor and to reduce the no-load losses in the motor. Nevertheless, increase in the length of air-gap increases the overload capacity, offers better cooling, reduces unbalanced magnetic pull and offers noise reduction. Therefore, there is need for an intelligent optimization to be adopted in the parent model to obtain high-speed operation with trade off of larger air-gap without affecting other performance features of the motor.

References

[1] F. O. Akpojedje, E. M. Okah and Y. O. Abu (2016). A Comparative Analysis of Three Phase Induction Motor Performance Evaluation. *International Journal of Engineering and Techniques*, Vol. 2(3), pp. 64-75.
[2] W. H. Ali, S. I. Abood and M. N. O. Sadiku (2019). Fundamentals of Electric Machines. CRC Press, London, UK.
[3] A. R. Khan and Q. Ahsan (2014). Development and Performance Analysis of a Two-Phase Induction Motor in the Frame and Core of a Single-Phase Induction Motor. *8th International Conference on Electrical and Computer Engineering*, Dhaka, Bangladesh, 20-22 December, 2014, pp. 469-472.
[4] S. Mandal (2015). Performance Analysis of Six-Phase Induction Motor. *International Journal of Engineering Research & Technology (IJERT)*, Vol. 4(2), pp. 589-593.
[5] G. S. Memon, M. A. Mahar, S. K. Guriro, C. Kumar and M. M. Shaikh (2018). Performance Analysis of Induction Motor Drive at Various Conduction Modes using 3-phase Bridge Inverter. *2018 IEEE 21st International Multi-Topic Conference (INMIC)*, Karachi, Pakistan, 1-2 November, 2018, pp. 206-212.
[6] M. Samir, G. Singh, N. Ahmed and H. Ahmed (2013). Dynamic Performance Analysis of Three Phase Induction Motor with Single Phasing. *Atlantis Press Conference on Advances in Communication and Control Systems 2013 (CAC2S 2013)*, Vol. 2013, pp. 216-221.
[7] J. F. Gieras (2017). Electrical Machines: Fundamentals of Electromechanical Energy. CRC Press, London, UK.
[8] S. N. Vukosavic (2013). Electrical Machines, Power Electronics and Power Systems. Springer Science Business Media, New York, USA.
[9] V. K. Mehta and R. Mehta (2009). *Principles of* Electrical Machines. *2nd Edition.* S. Chand & Company Ltd, Ram Nagar, New Delhi, India.
[10] S. K. Sahdev (2018). Electrical Machines. Cambridge University Press, United Kingdom.
[11] J. B. Gupta (2015). Theory and Performance of Electrical Machines. 15th Edition. S. K. Katara & Sons, Delhi, India.
[12] M. Ojaghi, M. Sabouri and J. Faiz (2018). Performance Analysis of Squirrel-Cage Induction Motors Under Broken Rotor Bar and Stator Inter-Turn Fault Conditions Using Analytical Modeling. *IEEE Transactions on Magnetics*, Vol. 54(11), pp. 1-5.
[13] R. Krishnan (2001). Electric Motor Drives Modeling, Analysis, and Control. Prentice Hall, Inc., Upper Saddle River, New Jersey, USA.
[14] T. Wildi (2002). Electrical Machines, Drives, and Power Systems. 5th Edition. Pearson Education Inc., Upper Saddle River, New Jersey, USA.

[15] P. C. Sen (2014). Principles of Electric Machines and Power Electronics. 3rd Edition. John Wiley & Sons, Inc., New Jersey, USA.
[16] B. S. Guru and H. R. Hiziroglu (2001). Electric Machinery and Transformers. 3rd Edition. Oxford University Press, Inc., New York, USA.
[17] T. Gonen (2012). Electrical Machines with Matlab. 2nd Edition. CRC Press, Boca Raton, London, UK.
[18] X. Li, Q. Wu and S. Nandi (2007). Performance Analysis of a Three-Phase Induction Machine with Inclined Static Eccentricity. *IEEE Transactions on Industry Applications*, Vol. 43(2), pp. 531-541.
[19] O. S. Olaleye, C. O. Ahiakwo, D. C. Idoniboyeobu and S. Orike (2020). Modeling of Eccentricity and Performance of Three-Phase Induction Motors. *Journal of Newviews in Engineering and Technology (JNET)*, Vol. 2(1), pp. 97-108.
[20] C. Ai, X. Cao and H. Wang (2021). Analysis of a 1.5kW Induction Motor Through Electromagnetic and Thermal Simulations. *3rd Asia Energy and Electrical Engineering Symposium*, Chengdu, China, 26-29 March, 2021, pp. 249-254.
[21] V. Fireteanu, A. Constantin and C. Dumitru (2021). Finite Element Analysis of the Performance of the 3-Phase, 5-Phase, 7-Phase and 9-Phase Squirrel-Cage Induction Motors. *The 12th International Symposium on Advanced Topics in Electrical Engineering*, Bucharest, Romania, 25-27 March, 2021, pp. 1-6.
[22] R. Pandey, A. K. Panda and N. Patnaik (2020). Comparative Performance Analysis of DTC fed Three-Phase and Five-Phase Induction Motor. *2020 5th International Conference on Devices, Circuits and Systems (ICDCS)*, Coimbatore, India, 5-6 March, 2020, pp. 162-166.
[23] J. R. Kumar and B. Banakara (2017). Finite Element Analysis in the Estimation of Air-Gap Torque and Surface Temperature of Induction Machine. *IOP Conference Series: Materials Science and Engineering*, Vol. 225, pp. 1-12.
[24] X. Wang, C. Zhu, R. Zhang, R. Tang and H. Song-Yop (2006). Performance Analysis of Single-Phase Induction Motor Based on Voltage Source Complex Finite-Element Analysis. *IEEE Transactions on Magnetics*, Vol. 42(4), pp. 587-590.
[25] E. C. Abunike, O. I. Okoro and G. D. Umoh (2017). Steady and Dynamic State Analysis of Induction Motor: FEA Approach. *Nigerian journal of Technology (NIJOTECH)*, Vol. 36(4), pp. 1202-1207.
[26] E. C. Abunike, P. I. Obi and N. J. Affia (2019). Stability Analysis of a Three-Phase Induction Motor under Asymmetrical Fault Conditions Using FEA Simulations. *IOSR Journal of Engineering (IOSRJEN)*, Vol. 9, No. 10, pp. 1-10.
[27] K. N. Ukoima, P. I. Obi and C. S. Ezeonye (2019). Dynamic Modelling of Excitation and Governor Effect on Stability of Electrical Machines. *2nd International Engineering Conference, IECON 2019*, Umudike, Nigeria, 2-4 September, 2019, pp. 1-11.